Ultrathin $LiCoO_2$ Nanosheets: An Efficient Water-Oxidation Catalyst

Jianghao Wang,[a] Liping Li,[b] Haiquan Tian,[a] Yuelan Zhang,[b] Xiangli Che,[a] Guangshe Li*[a, b]

[a] J. Wang, H. Tian, X. Che, Dr. G. Li
Fujian Institute of Research on the Structure of Matter University of Chinese Academy of Sciences
Fuzhou 350002, P. R. China

[b] Dr. G. Li, Dr. L. Li, Y. Zhang
State Key Laboratory of Inorganic Synthesis & Preparative Chemistry, College of Chemistry, Jilin University
Changchun 130012, P. R. China
E-mail: Guangshe@fjirsm.ac.cn; guangshe@jlu.edu.cn

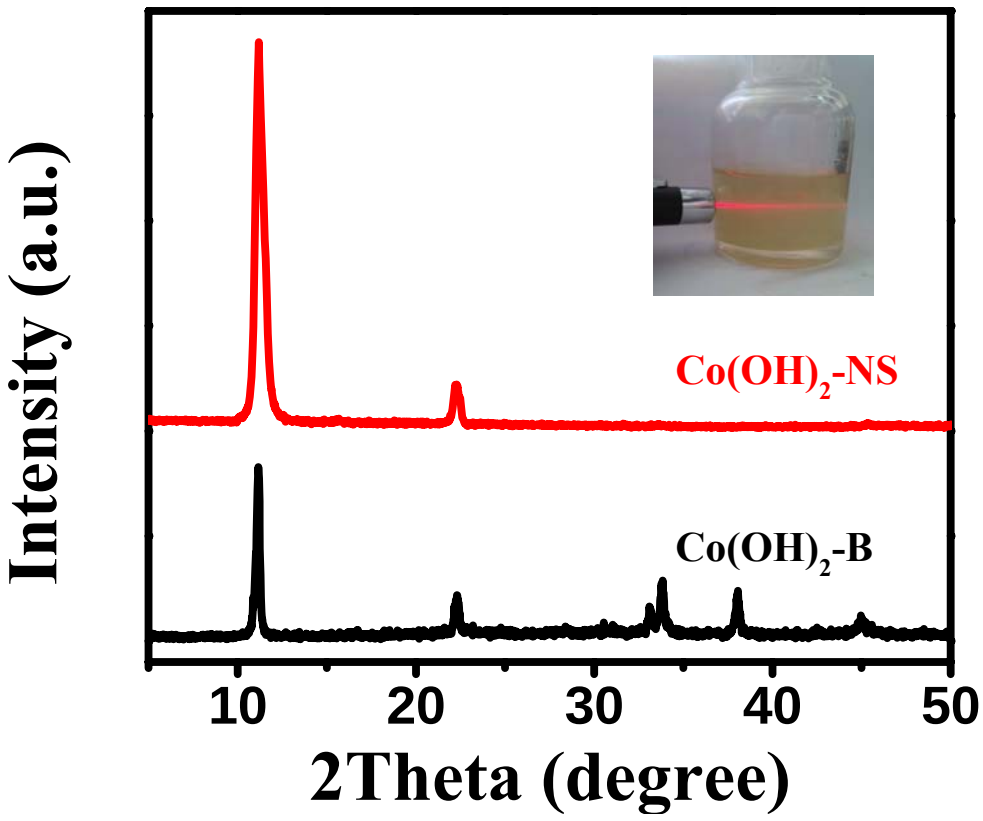

Figure S1. XRD pattern of $Co(OH)_2$-NS and $Co(OH)_2$-B. Inset shows the photograph of the corresponding colloidal dispersion that display the Tyndall effect.

As well known, it is infeasible to perform X-ray diffraction pattern (XRD) characterization on an individual nanosheet. Therefore, XRD pattern was recorded for an ultrathin nanosheet-based film which was fabricated by a layer-by-layer assembly strategy. As shown in Figure S1, the ultrathin $Co(OH)_2$-nanosheet-based film displayed a highly preferred (001) orientation without any desirable impurity peak. The clear Tyndall light scattering is discerned for the colloidal suspension, which reasonably indicates a large amount of $Co(OH)_2$ nanosheets dispersed in solution. All diffraction peaks of bulk-phase in this pattern can be indexed to α-$Co(OH)_2$, as reported in ref. [1]

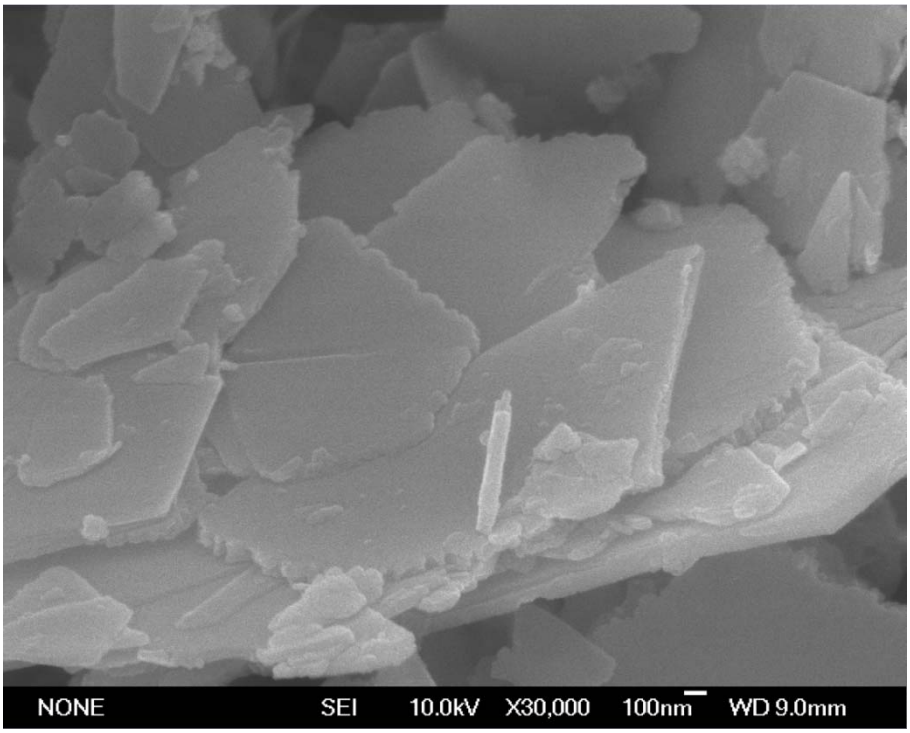

Figure S2. High magnification SEM image of the as-obtained $Co(OH)_2$-B.

Typical SEM images shown in Figure S2 reveal that $Co(OH)_2$-B displayed a plate-like morphology, consistent with those previously reported. The width of sheets was in the ranges of 2-3 μm, and the thickness of plates was about 50-60 nm.

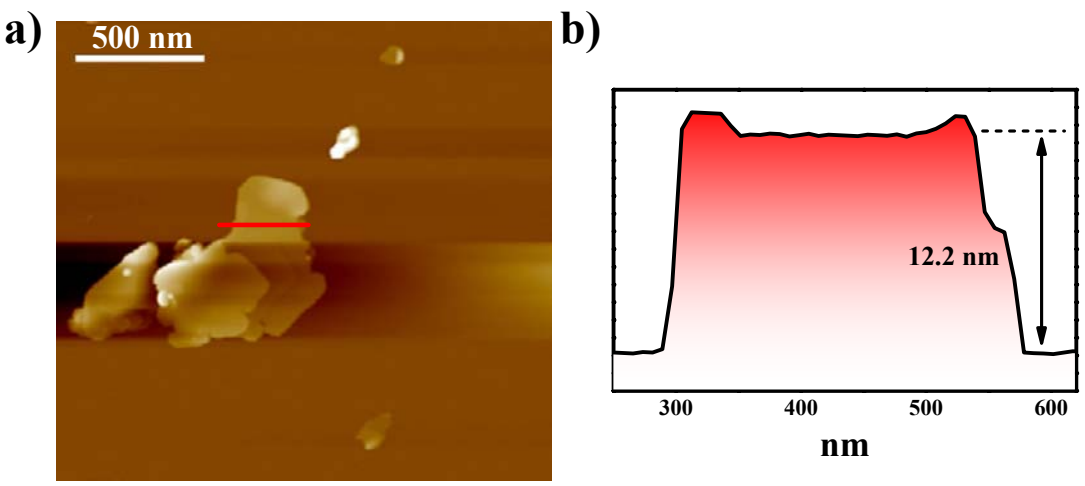

Figure S3. (a) and (b): Tapping mode AFM image and the corresponding height profile of the as-obtained α-$Co(OH)_2$ nanosheets deposited on a mica substrate. The height profile was corresponding to the height of nanosheets. The bar in (a) is 500 nm.

AFM image shows that the thickness of $Co(OH)_2$-NS was about 12.2 nm (about 5 Co layers), which provides a direct evidence for the successful exfoliation of $Co(OH)_2$-B. Moreover, the number of $Co(OH)_2$ layers was corresponding to the $LiCoO_2$-NS layers.

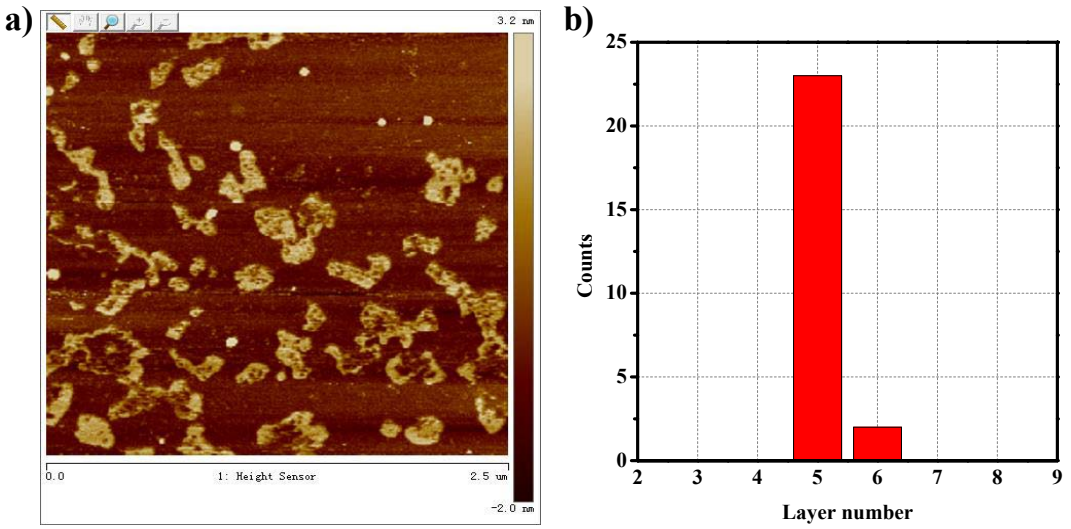

Figure S4. a) Tapping mode AFM image of $LiCoO_2$-NS, b) the thickness distribution of $LiCoO_2$ nanosheets.

All thickness of $LiCoO_2$ nanosheets in Figure S4 is distributed in a range, 2.2-2.8 nm. Taking into the consideration that one Co-O layer thickness is about 0.46 nm, we can infer that the thickness $LiCoO_2$ nanosheets we obtained is about five to six layers of Co-O layers.

Figure S5. Photograph of a colloidal suspension of the $LiCoO_2$-NS displaying the Tyndall effect.

The well-defined Tyndall effect of the $LiCoO_2$-NS solution as displayed in the inset of Figure S5 indicates the presence of highly monodispersed ultrathin nanosheets in water.

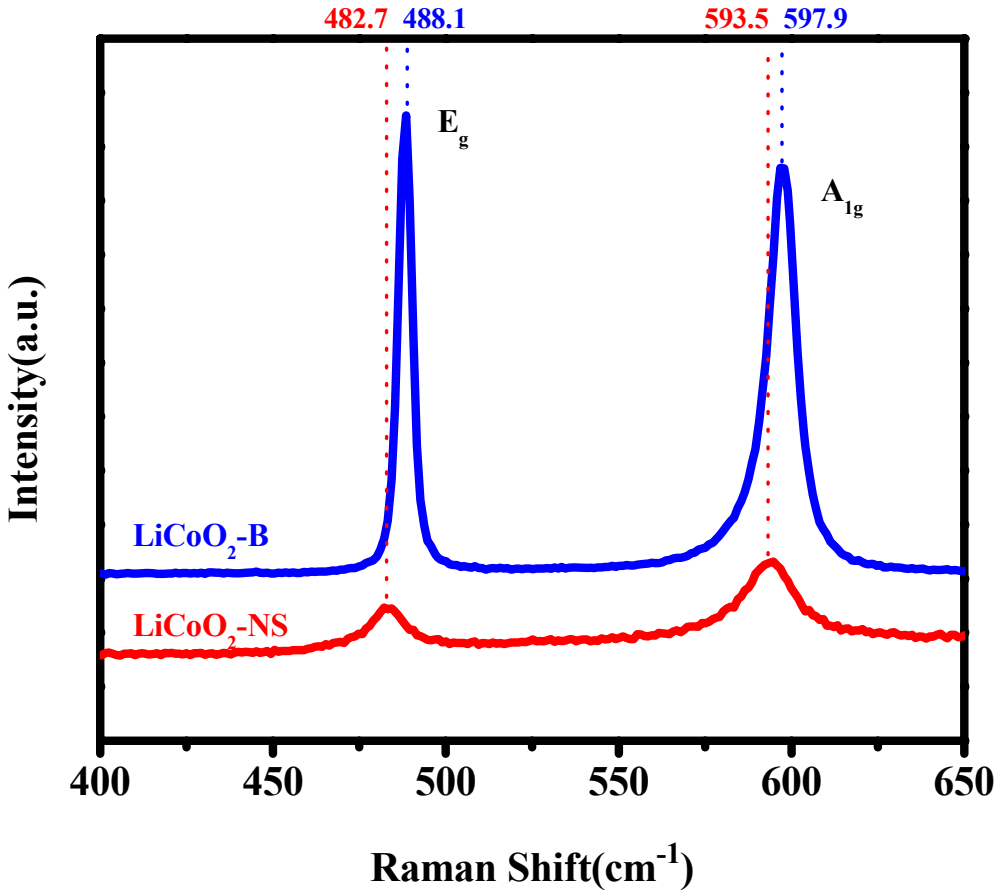

Figure S6. Raman spectra for $LiCoO_2$-NS and $LiCoO_2$-B.

For the layered structure, these are the $A_{1g}+E_g+2A_{2u}+2E_u$, among which A_{1g} and E_g bands are Raman-active. Two active Raman bands of the layered structure, at 593.7 and 483.2 cm^{-1}, correspond to A_{1g} and E_g.[2] Obviously, when compared to the bulk counterpart, the Raman bands shifted towards the lower wavenumbers, which could be ascribed to the phonon confinement effect associated with the ultrathin thickness feature.

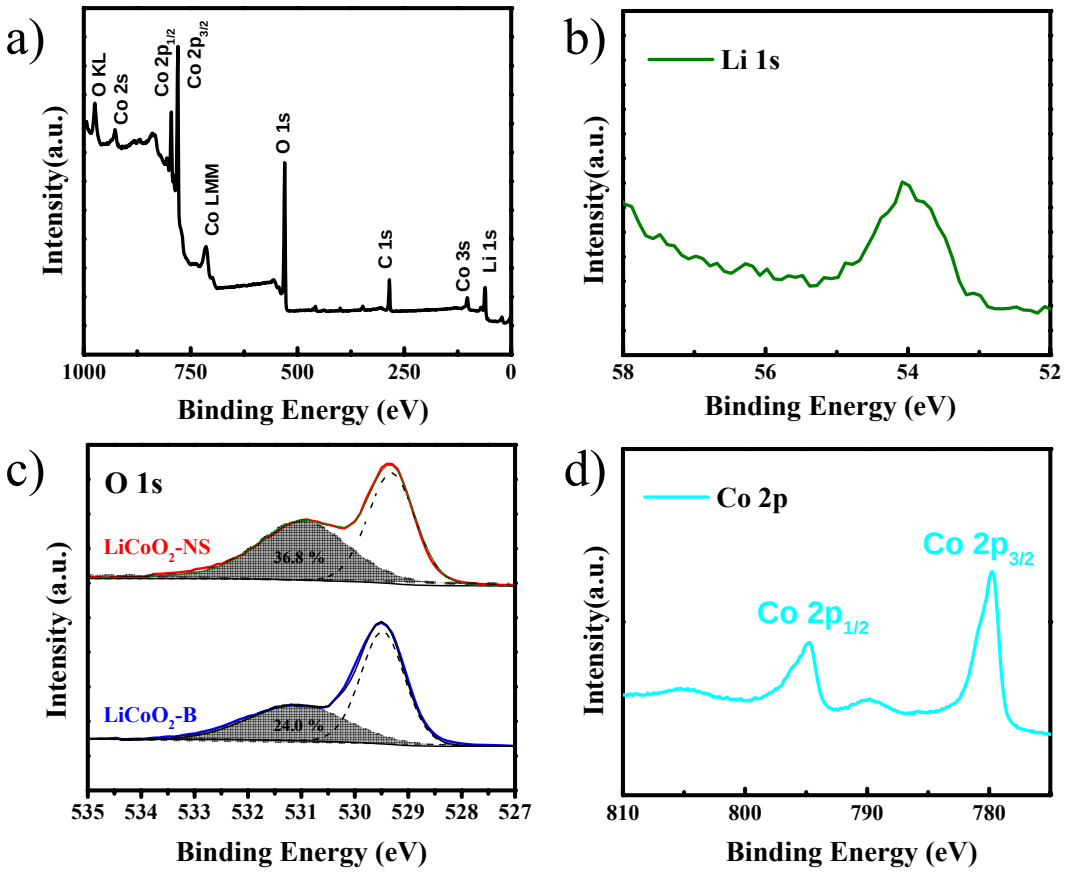

Figure S7. XPS spectra of $LiCoO_2$-NS: (a) XPS survey of various elements; (b) high resolution Li 1s XPS spectra, (c) high resolution O 1s XPS spectra, and (d) high resolution Co 2p XPS spectra.

O 1s core level spectra can be deconvoluted into two peaks: one at 529.4 eV is ascribed to the oxygen atoms bound to metals, while another at 531.0 is attributed to the surface oxygen species such as hydroxyls that might be absorbed at oxygen vacancy site. In addition, full width at half maximum (FWHM) of Co $2p_{3/2}$ peak in $LiCoO_2$-NS is 2.25 eV, which is broadened when comparing to 1.95 eV for bulk $LiCoO_2$.[3] These facts observed suggest that Co ions in $LiCoO_2$-NS should be in a mixed valence state. The valence and electronic state of $LiCoO_2$-NS were further demonstrated by temperature-dependent magnetic susceptibilities.

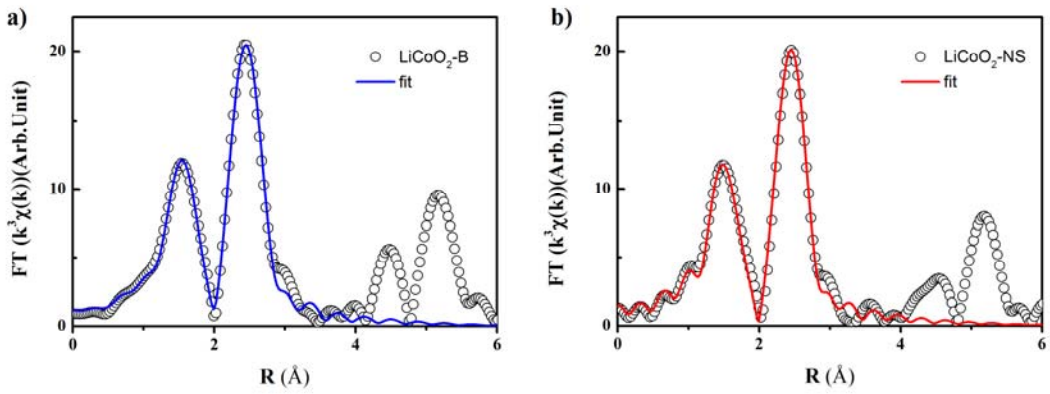

Figure S8. EXAFS curves-fitting result of the sample: (a) bulk and (b) nanosheet $LiCoO_2$.

Table S1. Structural parameters around Co atoms determined by fitting EXAFS data for $LiCoO_2$-B and $LiCoO_2$-NS.

Sample	Path	N	R (Å)	$\sigma^2(10^{-3}Å^2)$	ΔE_0 (eV)
$LiCoO_2$	Co-O	6.0	1.94	-	-
Theory	Co-Co	6.0	2.86	-	-
$LiCoO_2$	Co-O	6.0	1.92	2.9	-3.2
Bulk	Co-Co	6.0	2.82	2.7	-6.1
$LiCoO_2$	Co-O	5.8	1.90	3.1	-4.0
Nanosheets	Co-Co	5.8	2.81	3.0	-8.2

To compare the bonding length and coordination number of the nearest Co-O and next nearest Co-Co for $LiCoO_2$-B and $LiCoO_2$-NS, their EXAFS data were processed according to the standard procedures using ATHENA and ARTEMIS module implemented in the IFEFFIT software packages. The obtained data are listed in Table S1, which include the coordination number (N) of Co ion, average bonding length (R), Debye-Waller factor (σ^2) and edge-energy shift (ΔE_0). The distances and coordination number of $LiCoO_2$-NS reduced remarkably, when comparing to the theoretical value as well as that of $LiCoO_2$-B, suggesting an increase of disorder due to surface distortion.

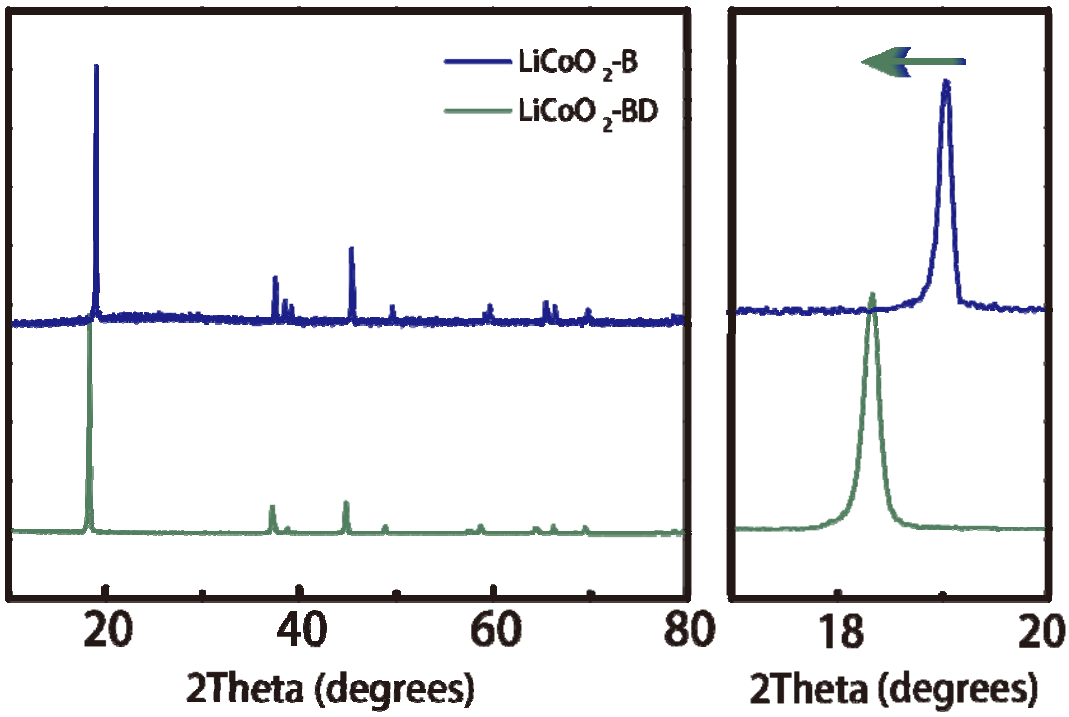

Figure S9. Powder XRD patterns of $LiCoO_2$-B and $LiCoO_2$-BD.

(003) peak disappeared at 2θ=19.0°, while a new peak appeared at 18.4°, which are the most obvious changes before and after delithiation. This result is in line with the results reported in literature.[4]

Table S2. OER performances of the samples relative to those of other typical samples reported in literature

catalyst	Loading (mg cm^{-2})	electrolytes	Onset overpotential (mV)	Overpotential @10 mA cm^{-2} (mV)
$LiCoO_2$-NS*	0.10	0.1M KOH	300	410
$LiCoO_2$-BD*	0.10	0.1M KOH	360	510
$LiCoO_2$-B*	0.10	0.1M KOH	400	—
LT-$LiCoO_2$[5]	0.25	0.1M KOH	330	470
Fe-Co_3O_4[6]	0.12	0.1M KOH	349	486
Co_3O_4-$CuCo_2O_4$[7]	0.12	0.1M KOH	321	498
Zn-Co-LDH/CNT[8]	0.28	0.1M KOH	340	548
Zn-Co-LDH nanosheets[9]	0.21	0.1M KOH	230	480
Mn_3O_4/$CoSe_2$[10]	0.20	0.1M KOH	—	450
Pt-$LiCoO_2$[11]	0.07	0.1M KOH	340	440
CoO/CNT[12]	0.15	0.1M KOH	320	390-450
Co_3O_4/Ni foam[13]	1.00	1.0M KOH	—	320-380
Co_3O_4/C[14]	0.20	1.0M KOH	240	290
Porous Co_3O_4[15]	0.10	0.1M KOH	—	410-450

Notes and references

(1) Liu, Z.; Ma, R.; Osada, M.; Takada, K.; Sasaki, T. Selective and Controlled Synthesis of α- and β-Cobalt Hydroxides in Highly Developed Hexagonal Platelets. *J. Am. Chem. Soc.* **2005**, *127* (40), 13869–13874.

(2) Okubo, M.; Hosono, E.; Kim, J.; Enomoto, M.; Kojima, N.; Kudo, T.; Zhou, H.; Honma, I. Nanosize Effect on High-Rate Li-Ion Intercalation in $LiCoO_2$ Electrode. *J. Am. Chem. Soc.* **2007**, *129* (23), 7444–7452.

(3) Yu, C.; Guan, X.; Li, G.; Zheng, J.; Li, L. A Novel Approach to Composite Electrode 0.3Li2MnO3–0.7LiMn1/3Ni1/3Co1/3O2 in Lithium-Ion Batteries with an Anomalous Capacity and Cycling Stability at 45.4°C. *Scr. Mater.* **2012**, *66* (5), 300–303.

(4) Lu, Z.; Wang, H.; Kong, D.; Yan, K.; Hsu, P.-C.; Zheng, G.; Yao, H.; Liang, Z.; Sun, X.; Cui, Y. Electrochemical Tuning of Layered Lithium Transition Metal Oxides for Improvement of Oxygen Evolution Reaction. *Nat. Commun.* **2014**, *5*, 4345-4351.

(5) Maiyalagan, T.; Jarvis, K. A.; Therese, S.; Ferreira, P. J.; Manthiram, A. Spinel-Type Lithium Cobalt Oxide as a Bifunctional Electrocatalyst for the Oxygen Evolution and Oxygen Reduction Reactions. *Nat. Commun.* **2014**, *5*, 3949-3956.

(6) Grewe, T.; Deng, X.; Tüysüz, H. Influence of Fe Doping on Structure and Water Oxidation Activity of Nanocast Co_3O_4. *Chem. Mater.* **2014**, *26* (10), 3162–3168.

(7) Grewe, T.; Deng, X.; Weidenthaler, C.; Schüth, F.; Tüysüz, H. Design of Ordered Mesoporous Composite Materials and Their Electrocatalytic Activities for Water Oxidation. *Chem. Mater.* **2013**, *25* (24), 4926–4935.

(8) Zou, X.; Goswami, A.; Asefa, T. Efficient Noble Metal-Free (Electro)Catalysis of Water and Alcohol Oxidations by Zinc–Cobalt Layered Double Hydroxide. *J. Am. Chem. Soc.* **2013**, *135* (46), 17242–17245.

(9) Qiao, C.; Zhang, Y.; Zhu, Y.; Cao, C.; Bao, X.; Xu, J. One-Step Synthesis of Zinc–cobalt Layered Double Hydroxide (Zn–Co-LDH) Nanosheets for High-Efficiency Oxygen Evolution Reaction. *J Mater Chem A* **2015**, *3* (13), 6878–6883.

(10) Gao, M.-R.; Xu, Y.-F.; Jiang, J.; Zheng, Y.-R.; Yu, S.-H. Water Oxidation Electrocatalyzed by an Efficient Mn_3O_4/$CoSe_2$ Nanocomposite. *J. Am. Chem. Soc.* **2012**, *134* (6), 2930–2933.

(11) Su, C.; Yang, T.; Zhou, W.; Wang, W.; Xu, X.; Shao, Z. Pt/C–$LiCoO_2$ Composites with Ultralow Pt Loadings as Synergistic Bifunctional Electrocatalysts for Oxygen Reduction and Evolution Reactions. *J Mater Chem A* **2016**, *4* (12), 4516–4524.

(12) Seo, B.; Sa, Y. J.; Woo, J.; Kwon, K.; Park, J.; Shin, T. J.; Jeong, H. Y.; Joo, S. H. Size-Dependent Activity Trends Combined with in Situ X-Ray Absorption Spectroscopy Reveal Insights into Cobalt Oxide/Carbon Nanotube-Catalyzed Bifunctional Oxygen Electrocatalysis. *ACS Catal.* **2016**, *6* (7), 4347–4355.

(13) Esswein, A. J.; McMurdo, M. J.; Ross, P. N.; Bell, A. T.; Tilley, T. D. Size-Dependent Activity of Co_3O_4 Nanoparticle Anodes for Alkaline Water Electrolysis. *J. Phys. Chem. C* **2009**, *113* (33), 15068–15072.

(14) Ma, T. Y.; Dai, S.; Jaroniec, M.; Qiao, S. Z. Metal–Organic Framework Derived Hybrid Co_3O_4-Carbon Porous Nanowire Arrays as Reversible Oxygen Evolution Electrodes. *J. Am. Chem. Soc.* **2014**, *136* (39), 13925–13931.

(15) Jin Sa, Y.; Kwon, K.; Yeong Cheon, J.; Kleitz, F.; Hoon Joo, S. Ordered Mesoporous Co 3 O 4 Spinels as Stable, Bifunctional, Noble Metal-Free Oxygen Electrocatalysts. *J. Mater. Chem. A* **2013**, *1* (34), 9992–10001.